

Finding Black Holes with Black Boxes – Using Machine Learning to Identify Globular Clusters with Black Hole Subsystems

Ammar Askar^{1*}, Abbas Askar^{2†}, Mario Pasquato³ and Mirek Giersz⁴

¹*Department of Computer Science, College of Science, Purdue University, 305 N. University Street, West Lafayette, IN 47907, USA*

²*Lund Observatory, Department of Astronomy, and Theoretical Physics, Lund University, Box 43, SE-221 00 Lund, Sweden*

³*INAF, Osservatorio Astronomico di Padova, vicolo dell'Osservatorio 5, 35122 Padova, Italy*

⁴*Nicolaus Copernicus Astronomical Center, Polish Academy of Sciences, ul. Bartycka 18, 00-716 Warsaw, Poland*

Accepted XXX. Received YYY; in original form ZZZ

ABSTRACT

Machine learning is a powerful technique, becoming increasingly popular in astrophysics. In this paper, we apply machine learning to more than a thousand globular cluster (GC) models simulated as part of the ‘MOCCA-Survey Database I’ project in order to correlate present-day observable properties with the presence of a subsystem of stellar mass black holes (BHs). The machine learning model is then applied to available observed parameters for Galactic GCs to identify which of them that are most likely to be hosting a sizeable number of BHs and reveal insights into what properties lead to the formation of BH subsystems. With our machine learning model, we were able to shortlist 21 Galactic GCs that are most likely to contain a BH subsystem. We show that the clusters shortlisted by the machine learning classifier include those in which BH candidates have been observed (M22, M10 and NGC 3201) and that our results line up well with independent simulations and previous studies that manually compared simulated GC models with observed properties of Galactic GCs. These results can be useful for observers searching for elusive stellar mass BH candidates in GCs and further our understanding of the role BHs play in GC evolution. In addition, we have released an online tool that allows one to get predictions from our model after they input observable properties.

Key words: stars: black holes – globular clusters: general – methods: numerical – methods: statistical

1 INTRODUCTION

The use of machine learning is rapidly increasing in astronomy, with applications including the modeling of instrumental systematics (Gibson et al. 2012) and the classification of variable-stars with over 24% improvement over prior methodologies (Richards et al. 2011). Supervised machine learning models in astronomy have mostly been used on hand-labeled data in order to automate tedious tasks on large survey datasets. In this work, we demonstrate a different approach: we train models on realistic simulations and attempt inference on real data. Through our approach, we try to identify Galactic globular clusters (GCs) that are most likely to be harbouring a large number of stellar mass black holes (BHs). By identifying clusters that are likely to contain BHs, we hope to achieve two main goals. Firstly, our

findings will assist observers searching for stellar mass BHs by narrowing down their search space to a few likely candidate clusters. Secondly, we hope to better understand the dynamical history of clusters containing BHs by identifying and studying them individually.

The motivation for finding these clusters is brought on by the growing observational evidence that dense stellar systems like GCs contain stellar mass BHs. A few accreting BH candidates have been identified through radio and X-ray observations in the Galactic GCs M22 (Strader et al. 2012), M62 (Chomiuk et al. 2013), 47 Tuc (Miller-Jones et al. 2015; Bahramian et al. 2017) and M10 (Shishkovsky et al. 2018). Giersz et al. (2018) discovered a BH in the Galactic GC NGC 3201 from spectroscopically obtained radial velocity measurements of its main sequence companion star. Accreting BH candidates have also been identified in few extragalactic GCs mainly through X-ray observations (Maccarone et al. 2007; Barnard et al. 2008; Maccarone et al.

* E-mail: aaskar@purdue.edu

† E-mail: askar@astro.lu.se

2011; Barnard et al. 2011; Dage et al. 2018). Dynamical mass estimates for some Galactic GCs (Sollima et al. 2016) and several extragalactic GCs (Taylor et al. 2015) reveal the presence of a significant fraction of non-luminous matter in those GCs. Furthermore, an isolated stellar mass BH candidate in NGC 6553 was discovered through gravitational microlensing (Minniti et al. 2015). All these observational discoveries point towards the possibility that there could be many more undiscovered BHs in GCs.

Depending on the initial mass of a GC, up to thousands of BHs should have formed from the evolution of massive stars in these dense stellar systems within tens of millions of years. Whether or not a significant fraction of BHs is retained in GCs depends on the natal kicks which BHs receive and the escape velocity from the GC. Distribution of BH natal kicks is uncertain and weakly constrained (Fragos et al. 2009; Zhang et al. 2013; Wong et al. 2014; Zuo 2015; Mandel 2016; Mirabel 2017; Repetto et al. 2017; O’Shaughnessy et al. 2017; Wysocki et al. 2018; Adams et al. 2017; Mirabel 2017; Giacobbo & Mapelli 2018; Mapelli 2018). If BH natal kicks are as high as the natal kicks inferred for neutron stars (Mirabel et al. 2001; Repetto et al. 2012; Janka 2013) from proper motion of pulsars (Hobbs et al. 2005) then most BHs will escape the cluster. However, if BHs receive reduced kicks (Belczynski et al. 2002; Willems et al. 2005; Belczynski et al. 2006; Wong et al. 2012) then depending on their final mass, which increases for lower metallicity progenitor stars, (Heger & Woosley 2002; Mapelli et al. 2009; Belczynski et al. 2010; Zampieri & Roberts 2009; Mapelli et al. 2010; Fryer et al. 2012; Mapelli et al. 2013; Spera et al. 2015; Spera & Mapelli 2017) their BH retention fraction will be higher. Recently, Breen (2018) has suggested that nucleosynthesis in accretion discs around retained stellar mass BHs in the early evolution of GCs could account for present-day light element anticorrelations observed in GCs.

Even if BH retention fraction is high, the long-term survival of BHs in GCs has been debated in numerous studies. It had been postulated that BHs retained in GCs would segregate and form a dynamically decoupled subsystem where they would interact through strong encounters. This would result in their ejection from the GC within a billion years (Kulkarni et al. 1993; Sigurdsson & Hernquist 1993; Portegies Zwart & McMillan 2000). More recent numerical and theoretical works have shown that BH depletion might not be so efficient and in GCs with large initial half-mass relaxation times, a sizeable number of BHs can survive from few a Gyr up to a Hubble time and longer (Morscher et al. 2013; Sippel & Hurley 2013; Breen & Heggie 2013a,b; Heggie & Giersz 2014; Morscher et al. 2015; Giersz et al. 2015; Wang et al. 2016; Mapelli 2016; Rodriguez et al. 2016; Kremer et al. 2018c; Arca Sedda et al. 2018; Askar et al. 2018). More works have also explored the impact of high BH retention on the dynamical evolution and observational properties of star clusters (Merritt et al. 2004; Mackey et al. 2007, 2008; Downing et al. 2010; Banerjee et al. 2010; Banerjee & Kroupa 2011; Leigh et al. 2014; Ziosi et al. 2014; Peuten et al. 2016; Arca-Sedda 2016; Chatterjee et al. 2017; Webb et al. 2018; Weatherford et al. 2018; Pavlík et al. 2018; Banerjee 2018; Zocchi et al. 2018; Kremer et al. 2018a).

Using global observational properties to determine whether a particular GC could contain a large number of BHs remains challenging. Results from GC simulations that

retain a large number of BHs up to a Hubble time show that these clusters are typically characterized by relatively low central surface brightness values, large stellar core and half-light radii, and long half-mass relaxation times (Askar et al. 2018). However, such present-day observational properties are not unique to GC models with many BHs. Observational properties of GCs depend on their evolutionary history which is governed by their initial properties and GC models without too many BHs may also exhibit observational properties similar to models that sustain a large number of BHs. Building on the work presented in Arca Sedda et al. (2018) and Askar et al. (2018), we experiment with several supervised machine learning classifiers that are trained on the observational properties of nearly 1300 simulated star cluster models surviving up to 12 Gyrs (Askar et al. 2017). The purpose of these classifiers is to use these observational properties to identify whether a GC could be harbouring a BH subsystem. We use these classifiers with readily available global observational properties of Galactic GCs (Harris 1996, *updated 2010* and Baumgardt & Hilker 2018) to identify which of them could contain a BH system.

The rest of this paper proceeds as follows: In section 2, we provide information on GC simulation models that were used in this study and which of their observational properties were selected in order to train the classifier. In section 3, we provide details as to how the classifier was constructed and which machine learning algorithms were used. In section 4, we apply the classifier we have developed to results from N -body simulations and available observational data for Galactic GCs. The results are presented in Table A1 and Table A2. In section 5, we discuss results and pinpoint which Galactic GCs are most likely to contain many BHs and compare our results with previous studies. In Section 6 we give the conclusions and provide links to access to our publicly available code for classifying GC models with a BH subsystem.

2 GC SIMULATION MODELS

For the purpose of this study, we used results from numerical simulations of GC models that were carried out using the MOCCA code (Hypki & Giersz 2013; Giersz et al. 2013) as part of the MOCCA-Survey Database I (Askar et al. 2017) project. MOCCA is a code for simulating star clusters based on Hénon’s implementation of the Monte Carlo method (Hénon 1971; Stodolkiewicz 1982, 1986) to follow the long-term dynamical evolution of spherically symmetric stellar clusters.

Additionally, the MOCCA code utilizes prescriptions for stellar and binary evolution from the SSE/BSE codes (Hurley et al. 2000, 2002) to evolve each star and binary system. For computing the outcome of strong interactions involving two binaries or a binary and single star, MOCCA uses the FEWBODY code (Fregeau et al. 2004). MOCCA also implements a realistic treatment for escapees in tidally limited clusters based on Fukushige & Heggie (2000). Results from the MOCCA code have been extensively compared with results from direct N -body simulations of star clusters. There is a remarkable agreement in the evolution of global parameters and populations of specific objects (Giersz et al. 2008, 2013; Wang et al. 2016; Madrid et al. 2017), however

the MOCCA code is significantly faster than direct N -body codes. The speed of the Monte Carlo method and the implementation of additional processes makes MOCCA an ideal tool to simulate the realistic evolution of a large set of GC models.

The MOCCA-Survey Database I (Askar et al. 2017; Pasquato et al. 2018) project comprises nearly 2000 star cluster models that were simulated using the MOCCA code and span a wide range of initial conditions. The initial conditions of the simulated star cluster models are provided in Table 1 in (Askar et al. 2017). From these simulations about 1300 star cluster models survive up to 12 Gyrs (see Pasquato et al. 2018 for initial properties of GC models that survive up to 12 Gyrs). In this paper, we make use of various 12 Gyr properties of these 1300 models as features. From these models, 162 models contain more than 15 BHs at 12 Gyrs. Following Askar et al. (2018), these models are tagged as models with a BH subsystem (BHS). Models with fewer than 15 BHs are tagged as NO BHS models.

2.1 Feature Selection and Analysis

We use the following global properties to determine the presence of BH subsystems:

- Observational Half-Light Radius
- Central Surface Brightness
- Central Velocity Dispersion
- Total V-band Luminosity
- Median Relaxation Time
- Observational Core Radius

In particular, these features were chosen because these are common observed properties. For the Milky Way GCs, their values were readily available within two catalogues (Harris 1996, *updated 2010* and Baumgardt & Hilker 2018). For the simulated GC models, snapshots from MOCCA simulations provide details of each star in the system including its position, radial and tangential velocities, luminosity, radii and magnitudes. Using this data, it is possible to compute the total V-band luminosity, surface brightness and velocity dispersion profiles for the cluster models. The Principal Component Analysis (PCA) as detailed in subsection 2.2 revealed these to be the features that explained the most variance.

As detailed in Askar et al. (2018), in order to calculate the central surface brightness from the simulated models we use the infinite projection method described in Appendix B of Mashchenko & Sills (2005) to generate a surface brightness profile for the GC at 12 Gyr; determine the central value in units of V-band luminosity per square pc. The profile is also used to obtain the observational core and half-light radii. To obtain the central velocity dispersion from the simulated GC models, we use the value in the innermost bin of a line-of-sight (LOS) velocity dispersion profile (made using only luminous stars brighter than $M_V = 6$) from the 12 Gyr projected snapshot. The median relaxation time for the cluster models is computed using the total cluster luminosity and the half-light radius. The calculation is done in the same way as done for Galactic GCs in Harris (1996,

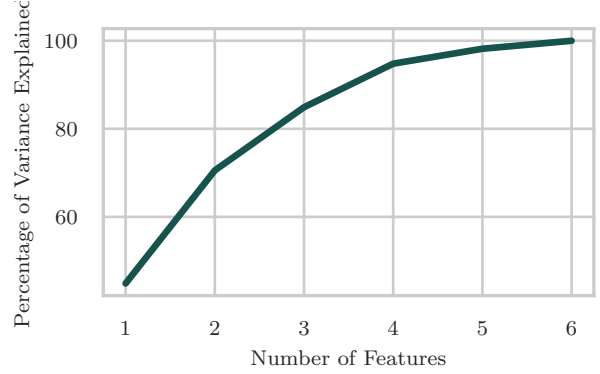


Figure 1. Number of features and the amount of variance they explain in the data as given with PCA analysis.

updated 2010)¹ using Equation 11 in (Djorgovski 1993):

$$t_{\text{rh}} = 2.055 \times 10^6 \text{ yr} \times \frac{1}{\ln(0.4N_*)} \langle m_* \rangle^{-1} (M_{\text{cl}})^{0.5} r_h^{1.5} \quad (1)$$

where M_{cl} (M_{\odot}) is the cluster mass estimated using the cluster V-band luminosity and assuming a mean mass-to-light ratio of 2. $\langle m_* \rangle$ (M_{\odot}) is the mean stellar mass which is assumed to be $1/3 M_{\odot}$ and N_* is the total number of stars which is found by dividing M_{cl} by $\langle m_* \rangle$. Following Harris (1996, *updated 2010*), we assume that r_h is the half-light radius in units of pc. Therefore, the median relaxation time (t_{rh}) essentially depends on the cluster luminosity and its half-light radius. We also trained the classifier on using the proper half-mass relaxation time (Spitzer 1987, Equation 2-62) at 12 Gyr from the simulated cluster models instead of the median relaxation time. This was done so that we could use the classifier with the catalogue of Galactic GC parameters provided by Baumgardt & Hilker (2018) (see Section 4 for details).

2.2 Principal Component Analysis

We performed PCA as outlined by Jolliffe (2011) on the data. This allows us to gain insight into how many features are required to explain the variance in the data in addition to figuring out the most important features. The percentage of variance explained by the number of features is presented in Figure 1.

The following steps were applied before performing the PCA analysis. The \log_{10} function was applied on the median relaxation time and central surface brightness. All features were then normalized by centering to the mean and standardizing to a unit variance.

The 3 features that explained the most variance were:

- Observational Core Radius
- Median Relaxation Time
- Central Surface Brightness

Pairwise plots of these features are presented in Figure 2. There seem to be some simple patterns that distinguish clusters with BH subsystems.

¹ See <http://physwww.mcmaster.ca/~harris/mwgc.ref> for details

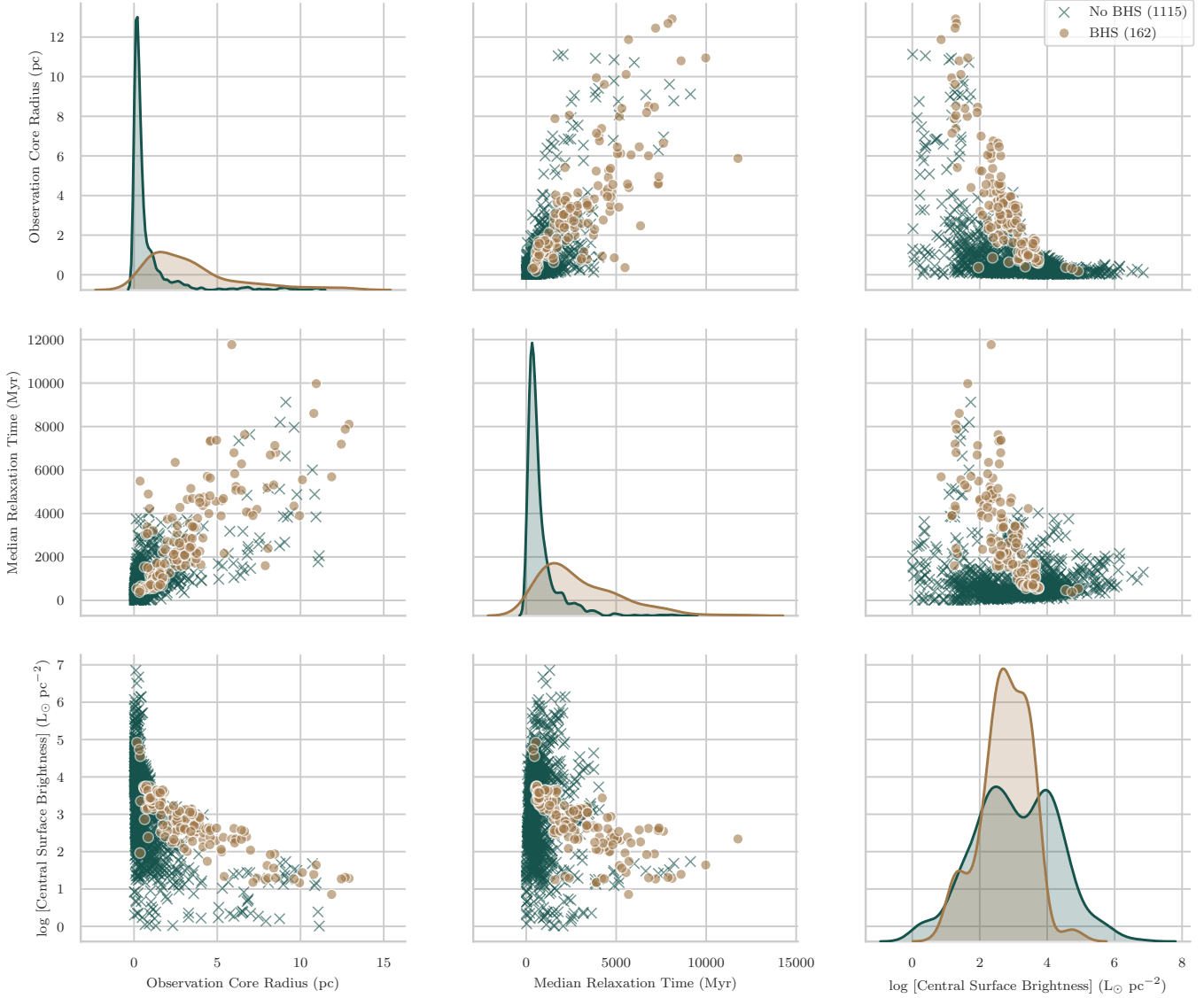


Figure 2. Pairwise plot of the 3 most important features. Each row and column represents a scatter plot between the two features. Matching rows and columns (diagonal panels) contain a distribution plot of the given observational parameter for cluster models with and without BH subsystems. A BHS containing cluster is defined as one that contains more than 15 BHs at 12 Gyr.

3 MACHINE LEARNING CLASSIFIER

The goal is to predict the presence of stellar mass BH subsystems (BHS) from the properties of a GC. We use supervised learning algorithms, that is, a model is trained upon data where we know whether a BHS is present or not. This model then makes predictions on data where their presence is unknown. A learning process tunes the model with the best possible parameters that minimize a cost function.

We use `scikit-learn` (Pedregosa et al. 2011) to evaluate different classification methods as well as XGBoost (Chen & Guestrin 2016) for the gradient boosted tree implementation. An empirical analysis of each classifier is presented, in particular we were after a model that offers good accuracy, minimizing false positives and one that we could analyze to uncover insights into what makes BH subsystems more likely to appear.

3.1 Naive Bayes

Naive Bayes classifiers are based on Bayes' theorem, using the training data to compute the conditional probabilities (Rish et al. 2001). By computing the prior probabilities and assuming their independence, we can compute the probability of a new data point x and its likelihood to be a member of a certain class C with:

$$p(C | x) \propto p(C) p(x_1 | C) p(x_2 | C) \dots \quad (2)$$

where x_1, x_2, \dots are the features of the new data point x and C is the predicted class.

The naivity in the name of the classifier is the assumption that the probabilities of each feature are independent, which is not necessarily true. In our case, one would expect, for example, the Central Surface Brightness and Core Ra-

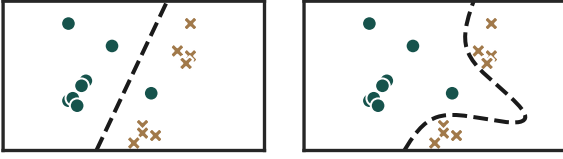


Figure 3. Example of linearity in SVM class boundaries with toy data. A less linear boundary may be able to fit the training data better but fail to generalize.

dus of a GC to be correlated. Hence, this classifier is mostly used as a baseline to evaluate the performance of others.

3.2 k-Nearest Neighbors

k-Nearest Neighbors is a simple classification technique that relies on a distance metric such as Euclidean distance or Manhattan distance and a hyper-parameter k explained below (Altman 1992).

Intuitively, kNN computes the distance between a new data point x with all the points in the training set x_i . The k points with the smallest distance are considered to be “closest” in value and the average of their labels is selected as the predicted label y for x .

3.3 Support Vector Machines

Support vector machines attempt to compute a hyperplane that separates the input data points if they were to be plotted in n dimensional space where n is the number of features (Hearst et al. 1998). We use hinge loss (Steinwart & Christmann 2008) which is defined as:

$$\max(0, 1 - y(\mathbf{w}^T \mathbf{x} + b)) \quad (3)$$

where \mathbf{w} and \mathbf{b} are the parameters of the hyperplane that need to be learned. y is the true class label, -1 if a BHS is not present or 1 if it is, \mathbf{x} are the features for the particular example. These hyperplanes can vary in linearity as seen in Figure 3 potentially trading off over-fitting and generalization.

3.4 Decision Trees

Decision trees (Quinlan 1986) are a powerful classification method that are relatively simple but can yield very good results especially for simpler models. As the name suggests, decision trees are a tree of “decisions”. These decisions could be, for example, whether the half light radius (R_e) is more than 2pc. The learning process finds decisions that split the input data in an attempt to minimize a loss function.

In particular, we use the Gini impurity (Venables & Ripley 2002) as the cost function:

$$1 - \sum_{j=1}^c p_j^2 \quad (4)$$

where p_j is the probability of a particular class being chosen at a given split. Thus, a split that completely divides the input set into two particular classes would result

in the probability of one class being 1 and the other being 0, resulting in the most minimum score of 0.

These splits are computed at every level of the tree until a max depth is reached, a certain Gini score is achieved or some other heuristic. The scores are computed at each decision making this a greedy algorithm.

One major advantage of decision trees is that they are not a complete black box, they can easily be introspected to reveal why the model makes certain decisions. This can be a very powerful tool to analyze the insights that the model might have generated.

3.5 Gradient Boosted Decision Trees

Gradient boosted decision trees attempt to improve on two of the major shortcomings of regular decision trees. Firstly, their tendency to overfit and secondly, offering a departure from a completely greedy approach.

Specifically, gradient boosting involves training dozens to hundreds of shallow decision trees and then aggregating their outputs with a set of weights to create a final prediction (Friedman 2002). Each tree is made to focus on the “mistakes” of previous trees by weighing samples that were mislabelled. Thus, the final classifier looks along the lines of:

$$f(x) = \sum_{i=1}^N \gamma_i g_i(x) \quad (5)$$

where N is the number of shallow trees trained, g_i is the output of the i th shallow tree and γ_i is the weight computed for it that minimizes the loss function.

Gradient boosted trees offer better accuracy than plain old decision trees because they can generate far more complex models (Roe et al. 2005). On the other hand, this makes them much more of a black box. It is hard to investigate and determine exactly why a certain prediction is being made one way or the other.

3.6 Scoring Metric And Testing

Classifiers were evaluated using stratified k-fold testing. Briefly, k-fold cross validation involves splitting up the training data into k overlapping subsets, within each of these subsets a portion of the data is used for testing and another portion for validation.

Stratified k-fold testing involves generating subsets that have a similar representation of classes as the input data set. If the original data has 30% true labels, then each subset will be chosen to have around 30% true values as well. As noted by Kohavi et al. (1995), this can result in far better bias and variance numbers when performing cross-validation.

Within each cross-validation test, a particular metric must be chosen to evaluate the performance of each classifier. In particular, we want a binary classification metric, since the problem we were trying to solve is whether a BH subsystem is present or not. A metric that is insensitive to imbalanced data is essential, since only around 12% of the simulated clusters have BH subsystems.

We also preferred metrics that weigh false-positives more aggressively than false-negatives. This allows us to single out good candidate clusters that can then be studied ob-

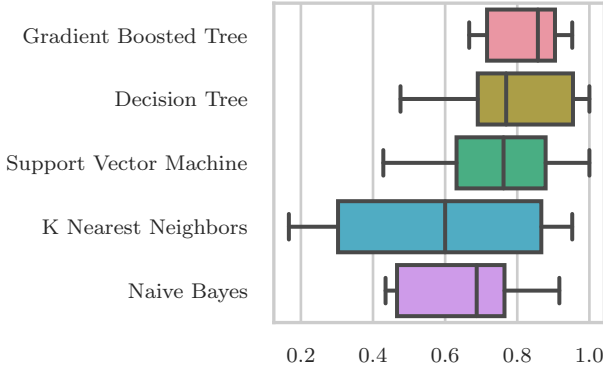


Figure 4. Comparison of each classifiers’ f-score with 15-fold testing. An f-score of 1.0 is the best possible, 0.0 is the worst. The score is affected by how well the classifier can find all the BH subsystems and whether the identifications are false-positives.

servationally to verify the presence of BH subsystems. Thus, we want to be very sure that the clusters classified are very likely to have a BH subsystem.

The metrics we looked at were:

- **Precision** (Davis & Goadrich 2006a)

$$\text{Precision} = \frac{tp}{tp + fp} \quad (6)$$

where tp is the number of true positives and fp is the number of false positives. Precision is the fraction of positive classifications that were actually correct. This metric ensures that we will be very confident if a BH subsystem is predicted, but we won’t necessarily be able to find all of them.

- **ROC-AUC** (Hanley & McNeil 1982)

The Receiving Operating Characteristic is a plot of the ratio of true positives and false positives. The area under this curve is an indicator of the classifier’s performance. The ROC curve is affected by true-negatives, which is problematic with our imbalanced data (Davis & Goadrich 2006b).

- **F-Score** (Sokolova et al. 2006)

The F-Score is the harmonic mean of precision and recall. Recall (Han et al. 2011) is defined as

$$\text{Recall} = \frac{tp}{tp + fn} \quad (7)$$

where tp is the number of true positives and fn is the number of false negatives. Recall ensures that we correctly classify all positive examples. Thus with f-score, we are confident there are not many false positives and that we manage to find all the clusters with BH subsystems.

F-Score was chosen as the metric to use in our situation since it aligns best with the objectives we noted above. In Figure 4 we present a comparison of the f-score of each classifier.

From the results, it is apparent that the decision trees offer the best performance characteristics. The gradient boosted trees have a slightly higher f-score and a smaller spread than regular decision trees. Hence, moving forward we decided to use both kinds of decision trees, offering results from the better performing gradient boosted trees and

Table 1. Ideal hyperparameters found for the decision tree classifier using random search with 15-fold verification with an f1 score of 0.798 ± 0.11

Hyperparameter	Description	Value
Max Depth	Maximum number of nodes from the root node down to a leaf of the tree.	5
Loss Function	Function to maximize for each split, either entropy gain or gini impurity decrease.	Gini
Max Features	The random subset of features to use when calculating splits. Used to reduce overfitting.	5
Min Split Sample	The minimum number of samples during a decision before creating a split.	2
Min Impurity Decrease	The minimum decrease in the loss function to create a split in the tree.	0.05

introspecting and presenting insights from the regular decision trees.

3.7 Tuning Hyperparameters and Analysing Classifiers

Machine learning algorithms rely on certain parameters which are not learned, but are instead provided by the user. For decision trees, this includes properties such as the max depth of the tree, the minimum change in the cost function and the number of trees used in gradient boosting. These hyperparameters are often tuned by hand based on heuristics about the data or they can be optimized computationally.

We used a technique known as “Random Searching” by Bergstra & Bengio (2012) in order to find the optimal hyperparameters. We used this over an exhaustive search such as a grid search (Bergstra et al. 2011) because it is much less computationally expensive.

Random searching involves randomly sampling values for each hyperparameter from a range, such as a max depth of a decision tree between 5 and 20. The classifier is then trained using these hyperparameters and k -fold testing is performed to evaluate which set of hyperparameters provide the best performance according to our scoring metric, f-score.

The search results for ideal hyperparameters are presented in Table 1 and Table 2, for decision trees and gradient boosted decision trees respectively. Confusion matrices (Fawcett 2006) are presented in Figure 5 and Figure 6. The confusion matrices offer a promising result, the amount of false positives is low for both the plain old decision trees and the gradient boosted trees.

3.8 Analysis of Decision Tree

A full visualization of the decision tree is presented in Figure A1. The first branching of the decision tree is based on core radius. Clusters with a small observational core radius are very unlikely to host BH subsystems, and this is reflected by

Table 2. Ideal hyperparameters found for gradient boosted decision tree classifier using random search with 15-fold verification with an f1 score of 0.857 ± 0.14

Hyperparameter	Description	Value
Loss Function	Function to minimize when choosing gradients and tree weights.	Mean Precision
Subsample	Percentage of samples to train base decision trees on.	100%
Estimators	The number of base decision trees to ensemble together.	850
Max Depth	Maximum number of nodes from the root down to a leaf in the decision trees.	6
Learning Rate	The factor to multiply the gradients by when performing gradient descent search.	0.3
Base Score	Initial weight for each training instance, the global bias.	0.5



Figure 5. Confusion matrix for decision tree classifier. The classifier was trained on a random 75% portion of the data. Predicted values were then tested for the remaining 25% against the real values, each value's categorization is then presented here.



Figure 6. Confusion matrix for gradient boosted tree classifier. The generation methodology is the same as for Figure 5.

the fact that 29 out of 963 (3%) of the clusters with $r_c < 1.15$ pc host a BH subsystem, as opposed to 162 out of 1289 for the whole simulation sample (12%). From a physical point of view, this is due to the presence of a BH subsystem which provides energy to surrounding luminous stars and prevents them from segregating in order to form a bright core. This results in a larger core radius value and lower central surface brightness. Following the bottom branch of the tree, where BH subsystem hosts are more abundant (133 out of 326, i.e. 37%), the next split is on total V-band luminosity. Simulated clusters with total luminosity above $2.6 \times 10^4 L_\odot$, which is a typical value for a small cluster such as NGC 2298, are more than ten times as likely to be BH subsystem hosts than smaller clusters (host fraction 69% compared to 6%). This result is also straightforward to interpret, as high present-day luminosity implies larger initial mass which increases the number of BHs that form in the cluster. A larger number of BHs can be retained in these clusters which also typically have longer initial relaxation times. Even if initial half-mass relaxation time is short for massive and dense clusters, they may still have a sizeable population of BHs at 12 Gyr. This is because BH retention fraction in the first 30 Myrs is higher due to large escape velocity from the dense cluster. Therefore, despite being dynamically older, such clusters may still contain comparable number of BHs at 12 Gyr to a dynamically younger GC model with a longer initial half-mass relaxation time. Further branches show that high central velocity dispersion is also an indicator of higher probability of being a BH subsystem host and so is low central surface brightness and long relaxation time, which are also expected based on our physical understanding of the dynamical effects of a BH subsystem (Arca Sedda et al. 2018).

4 PREDICTIONS USING MACHINE LEARNING

4.1 Predictions on results from N -body simulations

Before applying the classifier on available data for present-day structural parameters and properties available for Galactic GCs, we tested its efficacy by checking if it could determine the presence of a BH subsystem in GC models simulated with a direct N -body code instead of MOCCA. Wang et al. (2016) used the NBODY6++GPU (Wang et al. 2015) to simulate the evolution of four GC models with a million initial stars. The three models D1-R7-IMF93, D2-R7-IMF01 and D3-R7-ROT in Wang et al. (2016) were simulated up to 12 Gyr, at that time they had 245, 1037 and 1096 BHs respectively. We took the observational properties with which the classifier was trained from the 12 Gyr data available for those three models. The properties and the results from the classifier are shown in Table 3. For all the three GC models, the classifiers correctly predicted the presence of a BHS. This includes both the classifier that was trained on all MOCCA-Survey I GC models that survive up to 12 Gyr and the one that was trained only on simulated results in which mass fallback was enabled and BH kicks were lower.

Table 3. Predictions for the presence of BH subsystems with 12 Gyr data taken from the DRAGON million star GC direct N -body simulations (Wang et al. 2016) carried out using NBODY6++GPU (Wang et al. 2015)

Simulation Name	Half-Light Radius (pc)	Central Surface Brightness ($L_{\odot} \text{ pc}^{-2}$)	CVD ^a (km s ⁻¹)	Total V-band Luminosity (L_{\odot})	MRT ^b (Myr)	OCR ^c (pc)	BHS Prediction	BHS (Fallback)
D1-R7-IMF93	8.7	2.5×10^2	4.5	1.86×10^5	7417	4.8	True	True
D2-R7-IMF01	14.4	7.0×10^1	3.8	1.11×10^5	12706	10.0	True	True
D3-R7-ROT	13.4	1.3×10^2	4.0	1.22×10^5	11874	11.9	True	True

^aCentral Velocity Dispersion ^bMedian Relaxation Time ^cObservational Core Radius

4.2 Predictions on observational data for Galactic GCs

Having tested the trained classifier model described in the previous section on GC models simulated by Wang et al. (2016) using a direct N -body code, we then predicted whether stellar mass BHs were present in Galactic GCs using global observable properties from the Harris (1996, *updated 2010*) catalogue. This includes total V-band luminosity, half-light and core radius, central surface brightness, median relaxation time and central velocity dispersion. Similar to Askar et al. (2018), we applied the classifier to Galactic GCs that have Galactocentric radii smaller than 17 kpc. This was done because nearly 99 per cent of the GC models that had a BHS subsystem at 12 Gyr had Galactocentric radii smaller than 17 kpc. Distant Galactic GCs are not taken into account, this is because of the limited number of GC models with large Galactocentric distances in the MOCCA-Survey Database I models. Only three initial tidal radii values were taken in MOCCA-Survey Database I (Askar et al. 2017) and due to these limited initial parameters, no GC models with initial number of objects larger than 100,000 had Galactocentric radii larger than 20 kpc. The Harris (1996, *updated 2010*) catalogue does not provide central velocity dispersion for all Galactic GCs. For Galactic GCs in Harris (1996, *updated 2010*) where central velocity dispersion data was not available, we re-trained and used the classifier without this feature. One classifier was trained on all MOCCA-Survey I models that survived up to 12 Gyr and another classifier was trained on models in which mass fallback was enabled and BH kicks were lower. The observational properties that were used and the results from the classifiers for Harris (1996, *updated 2010*) catalogue data are provided in Table A1.

Additionally, we also used data for Galactic GC parameters provided by Baumgardt & Hilker (2018)². These parameters were obtained for 112 Galactic GCs by fitting a large grid of direct N -body simulations to the observed velocity dispersion and surface density profiles. In order to use our classifier on the data provided by Baumgardt & Hilker (2018), we converted cluster mass and central surface mass density³ to total V-band luminosity and central surface brightness using the mass-to-light ratio that they provided. The central surface brightness estimated from this data is an upper value as mass-to-light ratio is expected to be higher in the central part of the cluster due to segregated massive

compact remnants. Through their fitting procedure, Baumgardt & Hilker (2018) were also able to determine the half-mass relaxation time for the Galactic GCs in their catalogue. The classifier which was applied to data from Baumgardt & Hilker (2018) catalogue was thus trained on the half-mass relaxation time at 12 Gyr in our simulated cluster models instead of the median relaxation time (the classifier used for Harris (1996, *updated 2010*) catalogue data was trained on the median relaxation time). GC parameters and the results from the classifier for the Baumgardt & Hilker (2018) data are provided in Table A2.

Galactic GCs that were classified as having a BH subsystem in either one of the two catalogues (using either classifier trained on all models or only on fallback models) have been listed in Table 4. The green check marks indicate that the GC was classified as having a BHS. The columns indicate classification results from the two catalogues (Harris (1996, *updated 2010*) (marked as Harris) or Baumgardt & Hilker (2018) (marked as B&H)). Additionally, we distinguish where the classifier was trained on all models (BHS) and where it was trained only on models where mass fallback was enabled (Fallback). We have also indicated in Table 4 which of the clusters had been identified by Askar et al. (2018) as having a BH subsystem. Clusters which did not have a central velocity dispersion value in the Harris (1996, *updated 2010*) catalogue have also been indicated.

5 RESULTS - MILKY WAY GCS LIKELY TO CONTAIN BH SUBSYSTEM

Using the gradient boosted decision tree classifier and data from two different catalogues, we were able to shortlist 51 Galactic GCs that may contain a BH subsystem in Table 4. Out of these 51 clusters, 21 were identified in both Harris (1996, *updated 2010*) and Baumgardt & Hilker (2018) data sets. Among the 51 GCs that were identified by the machine learning classifier as having a BH subsystem, 27 of them had been previously identified by Askar et al. (2018) as having a BH subsystem. In their study, Askar et al. (2018) had identified 29 Galactic GCs that could contain a BH subsystem by manually comparing observational properties of MOCCA-Survey I models that had many BHs at 12 Gyr with the observed properties of Galactic GCs. Our automated approach is able to recover their findings and further identify additional GCs that could possibly contain a sizeable number of BHs. There were only 2 Galactic GCs identified by Askar et al. (2018) as having a BH subsystem that were not classified as having a BH subsystem in this study. These were NGC 6171 (M 107) and IC 276 (Pal 7). Both NGC 6171 and IC 276 have low central surface brightness and

² Data for GC parameters from Baumgardt & Hilker (2018) is available online at: <https://people.smp.uq.edu.au/HolgerBaumgardt/globular/>

³ See https://people.smp.uq.edu.au/HolgerBaumgardt/globular/combined_table.txt

Table 4. Predictions from the [Harris \(1996, updated 2010\)](#) and [Baumgardt & Hilker \(2018\)](#) datasets using the gradient boosted decision tree classifier. Entries where BHS presence was classified positively are shown. The *BHS* column represents the classifier trained on all simulation data whereas *Fallback* represents training on models where mass fallback was enabled and BH natal kicks were lower.

Cluster Name	BHS (Harris)	Fallback (Harris)	BHS (B&H)	Fallback (B&H)
IC 4499 *	✓	✓	✓	✓
NGC 288 *	✓	✓	✓	✓
NGC 3201 *	✓	✓	✗	✓
NGC 4372 *†	✓	✓	✓	✓
NGC 4590 (M68)	✗	✓	✗	✗
NGC 4833 *†	✗	✓	✓	✓
NGC 5139 (ω Cen)	✓	✓	✗	✓
NGC 5272 (M3) *	✗	✓	✓	✓
NGC 5286	✗	✓	✗	✓
NGC 5466 *	✗	✓	✗	✗
NGC 5897 *†	✓	✓	✗	✗
NGC 5904 (M5)	✗	✓	✓	✓
NGC 5927	✗	✗	✓	✓
NGC 5986 *†	✓	✓	✗	✓
NGC 6101 *†	✓	✓	✗	✗
NGC 6139 †	✓	✓	✗	✗
NGC 6144 *†	✗	✓	✓	✓
NGC 6205 (M13) *	✗	✓	✓	✓
NGC 6218 (M12)	✓	✓	✗	✗
NGC 6254 (M10)	✓	✓	✓	✓
NGC 6266 (M62)	✗	✗	✓	✗
NGC 6273 (M19) †	✗	✓	✓	✓
NGC 6287 †	✓	✓	✗	✗
NGC 6304 †	✗	✓	✓	✓
NGC 6316 †	✓	✓	✗	✗
NGC 6333 (M9) †	✓	✓	✗	✗
NGC 6356 †	✗	✓	✗	✓
NGC 6362 *	✗	✓	✗	✓
NGC 6380 †	✓	✓	✗	✗
NGC 6388	✗	✗	✓	✗
NGC 6401 *	✓	✓	✗	✗
NGC 6402 (M14) †	✓	✓	✓	✓
NGC 6426 *†	✗	✓	✗	✗
NGC 6440 †	✓	✓	✗	✗
NGC 6496 *†	✗	✓	✗	✗
NGC 6517 †	✗	✓	✗	✗
NGC 6539 (GCL 85)	✓	✓	✗	✗
NGC 6553	✓	✓	✗	✗
NGC 6569 *†	✓	✓	✓	✓
NGC 6584 *†	✓	✓	✗	✗
NGC 6656 (M22) *	✓	✓	✓	✓
NGC 6712 *	✗	✓	✓	✓
NGC 6723 *†	✓	✓	✓	✓
NGC 6760 †	✓	✓	✗	✗
NGC 6779 (M56) *	✗	✓	✓	✓
NGC 6809 (M55) *	✗	✓	✗	✓
NGC 6934 *	✓	✓	✗	✗
NGC 6981 (M72) *	✗	✓	✗	✗
NGC 7078 (M15)	✗	✗	✓	✓
NGC 7089 (M2)	✗	✓	✗	✓
Pal11 *†	✓	✓	✓	✓
Terzan5 †	✗	✓	✗	✗

* Clusters identified to contain BHS by [Askar et al. \(2018\)](#)

† Clusters without Central Velocity Dispersion data in Harris catalogue.

sufficiently long median relaxation time, however their observational core and half-light radii are not as large as other GCs identified as having a BH subsystem.

9 GCs were classified as having a BH subsystem with the classifier trained on all models as well as fallback models for both [Harris \(1996, updated 2010\)](#) and [Baumgardt & Hilker \(2018\)](#) catalogues. These clusters were IC 4499, NGC 288, NGC 4372, NGC 6254 (M10), NGC 6402 (M14), NGC 6569, NGC 6656 (M22), NGC 6723 and Pal 11. Among these, accreting BH candidates have been observed in NGC 6656 (M22) and NGC 6254 (M10) ([Strader et al. 2012](#); [Shishkovsky et al. 2018](#)).

After NGC 5139 (ω Cen), IC 4499 has the second largest half-mass relaxation time among all Galactic GCs within 17 kpc from the Galactic center in the [Baumgardt & Hilker \(2018\)](#) catalogue. The cluster has an unusually large core and half-light radii values that are consistent with GC models that contain a large number of BHs at a Hubble time. Among all Galactic GCs, NGC 3201's central surface brightness to total V-band luminosity ratio is one of the smallest. [Askar et al. \(2018\)](#) estimated that IC 4499 could contain few hundreds of BHs.

NGC 288 is another cluster which could contain a large population of BHs. [Sollima et al. \(2016\)](#) used extensive spectroscopic and photometric survey data to estimate the fraction of non-luminous mass within the half-light radius of NGC 288 and NGC 6218 (M12). They found that about 60 per cent of the mass inside the half-light radius could be in dark remnants. It may be possible that a significant amount of this unseen mass is in stellar mass BHs.

NGC 4372 is an old metal poor GC in the Galactic halo which has large core and half-light radii compared to most Galactic GCs. ([Kacharov et al. 2014](#)) carried out a detailed kinematic observations of NGC 4372 and found evidence for systematic rotation. They also obtained a half-light radius value lower than that reported in [Harris \(1996, updated 2010\)](#) and also provided the central velocity dispersion value. Using the parameters that they derived, the classifier still identified NGC 4372 is having a BH subsystem. Interestingly, [Servillat et al. \(2008\)](#) found 9 accreting X-ray sources in NGC 4372 and none of them were inside the half-light radius. Such close binary systems are expected to more centrally segregated due to their larger mass. Lack of segregation of such systems could point towards a population of more massive dark remnants in the central parts of NGC 4372.

Other Galactic GCs which were classified as having a BH subsystem in at least 3 columns shown in Table 4 were NGC 3201, NGC 4833, NGC 5139 (ω Cen), NGC 5272 (M3), NGC 5897, NGC 5904 (M5), NGC 6144, NGC 6205 (M13), NGC 6656 (M22), NGC 6712 and NGC 6779 (M56). Among these clusters, a BH in a detached binary has been observed in NGC 3201 ([Giesers et al. 2018](#)). Other accreting BH candidates have been observed in NGC 6266 (M62) and NGC 104 (47 Tuc). M62 has been classified as having a BH subsystem in Table 4 for parameters provided in the [Baumgardt & Hilker \(2018\)](#) catalogue. However, it not classified as having a BH subsystem when we use the parameters provided in the [Harris \(1996, updated 2010\)](#) catalogue. M62's total V-band luminosity in the [Baumgardt & Hilker \(2018\)](#) catalogue is almost half the value given in [Harris \(1996, updated 2010\)](#) catalogue. Also its half-mass relaxation time (~ 1350

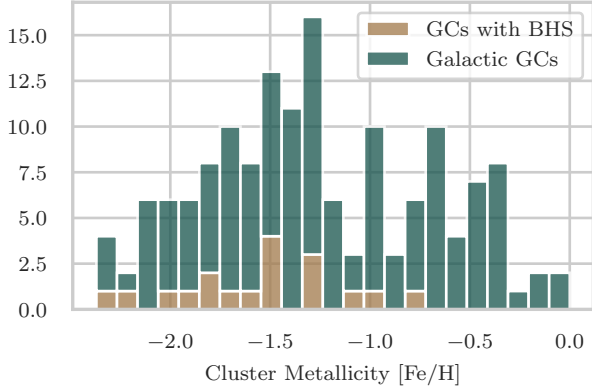


Figure 7. Distribution of cluster metallicities for all Milky Way GCs taken from the [Harris \(1996, updated 2010\)](#) catalogue in green. Metallicity distribution for Galactic GCs classified as having a BH subsystem with at least 3 ticks in [Table 4](#) are labeled with a different color.

Myr) in [Baumgardt & Hilker \(2018\)](#) is longer than the median relaxation time (~ 955 Myr) given in the [Harris \(1996, updated 2010\)](#) catalogue. Both M10 and M62 have small core and half-light radii compared to most GC models that have a BH subsystem. This could indicate that these GCs are depleting their BH population and evolving towards a second core bounce ([Brink et al. 2013](#)). During this phase of the cluster evolution, the size of the BH subsystem decreases while its density increases. This can lead to stronger dynamical interactions and it has been shown that a higher fraction of BHs in such clusters are in binaries and some of these could be mass transferring systems ([Kremer et al. 2018b](#); [Arca Sedda et al. 2018](#); [Askar et al. 2018](#)). Interestingly, M10 was considered as a possible candidate intermediate-mass black hole host by [Beccari et al. \(2010\)](#), even though their results were inconclusive.

In [Figure 7](#), we compared the metallicity distribution for the GCs that were classified as having a BH Subsystem for parameters provided in both [Harris \(1996, updated 2010\)](#) and [Baumgardt & Hilker \(2018\)](#) catalogues. Nearly all of these GCs are on the low metallicity end for GCs in the Milky Way. Metallicity plays an important role in the evolution of massive stars that are progenitors of BHs. Lower metallicity stars lose less mass due to stellar winds and produce more massive BHs ([Vink et al. 2001](#); [Belczynski et al. 2016](#); [Spera & Mapelli 2017](#)). If BH natal kicks depend on BH masses, then BHs that have low metallicity progenitors will have lower natal kicks. This can increase their retention fraction in GCs and therefore present-day GCs that are most likely to contain many BHs should have low metallicities. Moreover, if low metallicity GCs form more massive

Table 5. Galactic GCs classified as having a BH subsystem with at least 3 ticks in [Table 4](#) along with their metallicities.

Cluster Name	Metallicity [Fe/H]
IC 4499 *	-1.53
NGC 288 *	-1.32
NGC 3201 *	-1.59
NGC 4372 *	-2.17
NGC 4833 *	-1.85
NGC 5139 (ω Cen)	-1.53
NGC 5272 (M3) *	-1.5
NGC 5897 *	-1.9
NGC 5904 (M5)	-1.29
NGC 6144 *	-1.76
NGC 6205 (M13) *	-1.53
NGC 6254 (M10)	-1.56
NGC 6273 (M19)	-1.74
NGC 6304	-0.45
NGC 6402 (M14)	-1.28
NGC 6569 *	-0.76
NGC 6656 (M22) *	-1.7
NGC 6712 *	-1.02
NGC 6723 *	-1.1
NGC 6779 (M56) *	-1.98
Pal 11 *	-0.4

* Clusters identified to contain BHS by [Askar et al. \(2018\)](#)

BHs then the BH subsystem can keep the cluster in a state of balanced evolution ([Breen & Heggie 2013b](#)) for a longer time as massive BHs in binaries burn out slower ([Arca Sedda et al. 2018](#)). This can slow down the depletion of the BHs and delay the second core bounce ([Breen & Heggie 2013b](#)). In [Table 5](#), we provide a list of 21 Galactic GCs that are most likely to contain a BH subsystem based on ML classifier results on their available parameters in both [Harris \(1996, updated 2010\)](#) and [Baumgardt & Hilker \(2018\)](#) catalogues. The metallicities of these GCs taken from [Harris \(1996, updated 2010\)](#) are also shown in [Table 5](#).

It is important to point out that our results and the training of the classifiers significantly depends on how realistic our GC models are and how accurate are the observed parameters for Galactic GCs. While the simulated GC models take into account the most important physical processes that drive the dynamical evolution of GCs, there are other factors that could change present-day observational properties of GC models. This includes cluster rotation, proper treatment of the external tidal field and taking into account the clusters orbit (see [Askar et al. 2018](#) for a detailed discussion on limitations of using GC simulations to infer information about observed GCs).

For such a classifier to work properly, one needs strong constraints on the observed global properties of GCs. While many nearby Galactic GCs have been well studied, there can be many disagreements between values for distance, total luminosity, half-light and core radii between different studies. Obtaining parameters like central velocity dispersion or surface brightness through observations can be very challenging and usually these observed values can have significant errors. Results from the classifier can be sensitive to the values provided for the observable properties that were used as training features. For example, in [Table 4](#), NGC 7078 (M15) is classified as having a BH subsystem for parameters provided for it in the [Baumgardt & Hilker \(2018\)](#) catalogue. This is a dense

core collapsed cluster with a high central surface brightness value ($1 \times 10^5 L_{\odot} \text{pc}^{-2}$) in the Harris (1996, *updated 2010*) catalogue and one would not expect the presence of a BH subsystem in such a cluster. However, in the Baumgardt & Hilker (2018) catalogue, its central mass surface density ($\log(\Sigma_c)$ in units of $M_{\odot} \text{pc}^{-2}$) was just 0.45⁴ which resulted in it being classified as having a BH subsystem. Therefore, it is important to have correct values for such parameters in order for the classifier to properly work. Similarly, Terzan 5 is classified as having a BH subsystem for Harris (1996, *updated 2010*) data with the classifier trained only on models in which mass fallback was enabled. The GC has a compact dense core and a short median relaxation time. Therefore, it is not likely to contain a large number of BHs. However, its central surface brightness in Harris (1996, *updated 2010*) catalogue is about 3 orders of magnitude lower than the one in the Baumgardt & Hilker (2018) catalogue and for this reason it is classified as having a BH subsystem. For clusters like Terzan 5 which have a large colour excess ($E(B - V) \lesssim 2.82$ (Massari et al. 2012)), estimates of central surface brightness can have large errors. Moreover, the central surface brightness values provided in the Harris (1996, *updated 2010*) catalogue are mostly from ground-based imaging data, with spatial resolution of about 1 arcsecond⁵ and there could be large uncertainty in these values. With future telescopes and data releases from the *Gaia* mission, better observational data will be available for Galactic GCs. This will provide strong constraints on GC parameters which will be useful in determining whether they could contain a large population of BHs.

Apart from uncertainties in observational data, it is also important to point out the limitations in the simulated GC models. For MOCCA-Survey Database I GC models, the evolution of massive stars and final BH masses were based on prescriptions provided in the SSE/BSE (Hurley et al. 2000, 2002) codes. BH natal kicks were drawn from a Maxwellian distribution (with $\sigma = 265 \text{ km s}^{-1}$) (Hobbs et al. 2005) and in the fallback models, the kick magnitude depended on BH mass (Belczynski et al. 2002). Recent developments in wind prescriptions (Gräfenor et al. 2011), supernovae models (Fryer et al. 2012) and evolution of massive stars (including pair and pulsational instability supernovae (Belczynski et al. 2016; Spera & Mapelli 2017)) can strongly influence final BH masses and retention fractions in GCs. This can subsequently affect the evolution of the BH subsystem and how it shapes the global properties of the clusters. Therefore, results from future simulations with improved physics for evolution of BH progenitors will be useful in determining present-day properties of GCs that retain a large number of BHs. Moreover, other important factors such as distribution of the initial binary parameters (Belloni et al. 2017b), common envelope evolution (Belloni et al. 2017a; Giacobbo & Mapelli 2018) can also be important in determining compact object populations and present-day observational properties of GC models.

6 CONCLUSIONS

In this work, we applied machine learning in a new and novel way to astrophysics: predicting real world properties based on simulations. An empirical comparison was performed between multiple classifiers with the guiding metric primarily being a low false positive rate (f-score). We successfully trained a fairly accurate gradient boosted decision tree classifier on simulation data and then applied the learned model onto real world data. *K*-fold testing with our simulation data showed that the model had an accuracy of 95% and a false positive rate of less than 1%. Moreover, applying the classifier on an independent set of simulations (*N*-body vs Monte Carlo) yielded accurate results as well, a classifier trained on MOCCA Monte Carlo simulations was able to accurately predict the presence of BHS in *N*-body (Wang et al. 2016) simulated clusters using just the observational properties.

Applied onto real world data, our results are also fairly encouraging. We ran our model on two different catalogues of Milky Way GCs in order to get predictions based on independent data sets. We managed to successfully identify several clusters which have been ascertained to contain BHs by previous observational studies. This includes the likes of NGC 3201 as corroborated by Giesers et al. (2018), M22 (Strader et al. 2012) and M10 (Shishkovsky et al. 2018). In addition, our results match up closely with previous hand-crafted models on the same simulation data. Among the 29 Galactic GCs identified by hand in Askar et al. (2018), 27 were also identified by the machine learning classifier. We believe these results signal that this technique is fairly accurate and that the shortlisted clusters might be promising for observers to explore.

We have published our code publicly on Github for the sake of reproducibility and reference. Installation and usage instructions are distributed along with the code and can be found at github.com/ammaskar/black-holes-black-boxes. Additionally, the repository links to an interactive web page where one may put in their own observational values to get a prediction from the classifier. As better observational data for Galactic and extragalactic GC will become available in the future, the classifier can be used with updated observational properties to determine whether the GCs could contain a sizeable number of BHs.

In the future, we plan to run a large survey of simulated GC models for the MOCCA-Survey Database II with improved stellar/binary evolution prescriptions and initial binary parameter distribution. This will comprise several thousand GC models that will sample a wider range of initial GC parameters compared to MOCCA-Survey Database I. With results from those simulations, the ML classifier can be retrained to better identify GCs that could contain a large population of BHs using their present-day properties. Furthermore, this would also open up more avenues for ML applications, in particular a regression model could be trained to predict and approximate the number of compact objects in a cluster.

ACKNOWLEDGEMENTS

We are extremely grateful to Michela Mapelli for providing useful comments and suggestions that helped to improve

⁴ https://people.smp.uq.edu.au/HolgerBaumgardt/globular/combined_table.txt

⁵ <http://physwww.mcmaster.ca/~harris/mwgc.ref>

the manuscript. Many thanks are warranted for the scikit-learn community for creating such an extensive and useful open source project available for public consumption. AA(2) is supported by the Carl Tryggers Foundation through the grant CTS 17:113. MP and this project has received funding from the European Union's Horizon 2020 research and innovation programme under the Marie Skłodowska-Curie grant agreement No. 664931. MG acknowledge support from National Science Center (NCN), Poland, through the grant UMO-2016/23/B/ST9/02732. This work benefited from support by the International Space Science Institute (ISSI), Bern, Switzerland, through its International Team programme ref. no. 393 *The Evolution of Rich Stellar Populations & BH Binaries* (2017-18).

REFERENCES

- Adams S. M., Kochanek C. S., Gerke J. R., Stanek K. Z., Dai X., 2017, *MNRAS*, **468**, 4968
- Altman N. S., 1992, *The American Statistician*, **46**, 175
- Arca-Sedda M., 2016, *MNRAS*, **455**, 35
- Arca Sedda M., Askar A., Giersz M., 2018, *MNRAS*, **479**, 4652
- Askar A., Szkudlarek M., Gondek-Rosińska D., Giersz M., Bulik T., 2017, *MNRAS*, **464**, L36
- Askar A., Arca Sedda M., Giersz M., 2018, *MNRAS*, **478**, 1844
- Bahramian A., et al., 2017, *MNRAS*, **467**, 2199
- Banerjee S., 2018, *MNRAS*, **481**, 5123
- Banerjee S., Kroupa P., 2011, *ApJ*, **741**, L12
- Banerjee S., Baumgardt H., Kroupa P., 2010, *MNRAS*, **402**, 371
- Barnard R., et al., 2008, *ApJ*, **689**, 1215
- Barnard R., Garcia M., Li Z., Primini F., Murray S. S., 2011, *ApJ*, **734**, 79
- Baumgardt H., Hilker M., 2018, *MNRAS*, **478**, 1520
- Bayes T., 1763, [10.1098/rstl.1763.0053](https://doi.org/10.1098/rstl.1763.0053)
- Beccari G., Pasquato M., De Marchi G., Dalessandro E., Trenti M., Gill M., 2010, *ApJ*, **713**, 194
- Belczynski K., Kalogera V., Bulik T., 2002, *ApJ*, **572**, 407
- Belczynski K., Sadowski A., Rasio F. A., Bulik T., 2006, *ApJ*, **650**, 303
- Belczynski K., Bulik T., Fryer C. L., Ruiter A., Valsecchi F., Vink J. S., Hurley J. R., 2010, *ApJ*, **714**, 1217
- Belczynski K., et al., 2016, *A&A*, **594**, A97
- Belloni D., Zorotovic M., Schreiber M. R., Leigh N. W. C., Giersz M., Askar A., 2017a, *MNRAS*, **468**, 2429
- Belloni D., Askar A., Giersz M., Kroupa P., Rocha-Pinto H. J., 2017b, *MNRAS*, **471**, 2812
- Bergstra J., Bengio Y., 2012, *Journal of Machine Learning Research*, **13**, 281
- Bergstra J. S., Bardenet R., Bengio Y., Kégl B., 2011, in *Advances in neural information processing systems*. pp 2546–2554
- Breen P. G., 2018, *MNRAS*, **481**, L110
- Breen P. G., Hoggie D. C., 2013a, *MNRAS*, **432**, 2779
- Breen P. G., Hoggie D. C., 2013b, *MNRAS*, **436**, 584
- Brink H., Richards J. W., Poznanski D., Bloom J. S., Rice J., Negahban S., Wainwright M., 2013, *MNRAS*, **435**, 1047
- Chatterjee S., Morscher M., Rodriguez C. L., Pattabiraman B., Rasio F. A., 2017, in *Charbonnel C., Nota A., eds, IAU Symposium Vol. 316, Formation, Evolution, and Survival of Massive Star Clusters*. pp 234–239, [doi:10.1017/S1743921315010674](https://doi.org/10.1017/S1743921315010674)
- Chen T., Guestrin C., 2016, in *Proceedings of the 22nd ACM SIGKDD International Conference on Knowledge Discovery and Data Mining. KDD '16*. ACM, New York, NY, USA, pp 785–794, [doi:10.1145/2939672.2939785](https://doi.org/10.1145/2939672.2939785), <http://doi.acm.org/10.1145/2939672.2939785>
- Chomiuk L., Strader J., Maccarone T. J., Miller-Jones J. C. A., Heinke C., Noyola E., Seth A. C., Ransom S., 2013, *ApJ*, **777**, 69
- Dage K. C., Zepf S. E., Bahramian A., Kundu A., Maccarone T. J., Peacock M. B., 2018, *ApJ*, **862**, 108
- Davis J., Goadrich M., 2006a, in *Proceedings of the 23rd international conference on Machine learning*. pp 233–240
- Davis J., Goadrich M., 2006b, in *Proceedings of the 23rd international conference on Machine learning*. pp 233–240
- Djorgovski S., 1993, in *Djorgovski S. G., Meylan G., eds, Astronomical Society of the Pacific Conference Series Vol. 50, Structure and Dynamics of Globular Clusters*. p. 373
- Downing J. M. B., Benacquista M. J., Giersz M., Spurzem R., 2010, *MNRAS*, **407**, 1946
- Fawcett T., 2006, *Pattern recognition letters*, **27**, 861
- Fragos T., Willems B., Kalogera V., Ivanova N., Rockefeller G., Fryer C. L., Young P. A., 2009, *ApJ*, **697**, 1057
- Fregeau J. M., Cheung P., Portegies Zwart S. F., Rasio F. A., 2004, *MNRAS*, **352**, 1
- Friedman J. H., 2002, *Computational Statistics & Data Analysis*, **38**, 367
- Fryer C. L., Belczynski K., Wiktorowicz G., Dominik M., Kalogera V., Holz D. E., 2012, *ApJ*, **749**, 91
- Fukushige T., Hoggie D. C., 2000, *MNRAS*, **318**, 753
- Giacobbo N., Mapelli M., 2018, *MNRAS*, **480**, 2011
- Gibson N. P., Aigrain S., Roberts S., Evans T. M., Osborne M., Pont F., 2012, *MNRAS*, **419**, 2683
- Giersz M., Hoggie D. C., Hurley J. R., 2008, *MNRAS*, **388**, 429
- Giersz M., Hoggie D. C., Hurley J. R., Hypki A., 2013, *MNRAS*, **431**, 2184
- Giersz M., Leigh N., Hypki A., Lützgendorf N., Askar A., 2015, *MNRAS*, **454**, 3150
- Giesers B., et al., 2018, *MNRAS*, **475**, L15
- Gräfenor G., Vink J. S., de Koter A., Langer N., 2011, *A&A*, **535**, A56
- Han J., Pei J., Kamber M., 2011, *Data mining: concepts and techniques*. Elsevier
- Hanley J. A., McNeil B. J., 1982, *Radiology*, **143**, 29
- Harris W. E., 1996, *AJ*, **112**, 1487
- Hearst M. A., Dumais S. T., Osuna E., Platt J., Scholkopf B., 1998, *IEEE Intelligent Systems and their applications*, **13**, 18
- Heger A., Woosley S. E., 2002, *ApJ*, **567**, 532
- Hoggie D. C., Giersz M., 2014, *MNRAS*, **439**, 2459
- Hénon M. H., 1971, *Ap&SS*, **14**, 151
- Hobbs G., Lorimer D. R., Lyne A. G., Kramer M., 2005, *MNRAS*, **360**, 974
- Hurley J. R., Pols O. R., Tout C. A., 2000, *MNRAS*, **315**, 543
- Hurley J. R., Tout C. A., Pols O. R., 2002, *MNRAS*, **329**, 897
- Hypki A., Giersz M., 2013, *MNRAS*, **429**, 1221
- Janka H.-T., 2013, *MNRAS*, **434**, 1355
- Jolliffe I., 2011, in *International encyclopedia of statistical science*. Springer, pp 1094–1096
- Kacharov N., et al., 2014, *A&A*, **567**, A69
- Kohavi R., et al., 1995, in *Ijcai*. pp 1137–1145
- Kremer K., Chatterjee S., Ye C. S., Rodriguez C. L., Rasio F. A., 2018a, preprint, ([arXiv:1808.02204](https://arxiv.org/abs/1808.02204))
- Kremer K., Chatterjee S., Rodriguez C. L., Rasio F. A., 2018b, *ApJ*, **852**, 29
- Kremer K., Ye C. S., Chatterjee S., Rodriguez C. L., Rasio F. A., 2018c, *ApJ*, **855**, L15
- Kulkarni S. R., Hut P., McMillan S., 1993, *Nature*, **364**, 421
- Leigh N. W. C., Lützgendorf N., Geller A. M., Maccarone T. J., Heinke C., Sesana A., 2014, *MNRAS*, **444**, 29
- Maccarone T. J., Kundu A., Zepf S. E., Rhode K. L., 2007, *Nature*, **445**, 183
- Maccarone T. J., Kundu A., Zepf S. E., Rhode K. L., 2011, *MNRAS*, **410**, 1655

- Mackey A. D., Wilkinson M. I., Davies M. B., Gilmore G. F., 2007, *MNRAS*, **379**, L40
- Mackey A. D., Wilkinson M. I., Davies M. B., Gilmore G. F., 2008, *MNRAS*, **386**, 65
- Madrid J. P., Leigh N. W. C., Hurley J. R., Giersz M., 2017, *MNRAS*, **470**, 1729
- Mandel I., 2016, *MNRAS*, **456**, 578
- Mapelli M., 2016, *MNRAS*, **459**, 3432
- Mapelli M., 2018, preprint, ([arXiv:1809.09130](https://arxiv.org/abs/1809.09130))
- Mapelli M., Colpi M., Zampieri L., 2009, *MNRAS*, **395**, L71
- Mapelli M., Ripamonti E., Zampieri L., Colpi M., Bressan A., 2010, *MNRAS*, **408**, 234
- Mapelli M., Zampieri L., Ripamonti E., Bressan A., 2013, *MNRAS*, **429**, 2298
- Mashchenko S., Sills A., 2005, *ApJ*, **619**, 243
- Massari D., et al., 2012, *ApJ*, **755**, L32
- Merritt D., Piatek S., Portegies Zwart S., Hemsendorf M., 2004, *ApJ*, **608**, L25
- Miller-Jones J. C. A., et al., 2015, *MNRAS*, **453**, 3918
- Minniti D., et al., 2015, *ApJ*, **810**, L20
- Mirabel F., 2017, *New Astron. Rev.*, **78**, 1
- Mirabel I. F., Dhawan V., Mignani R. P., Rodrigues I., Guglielmetti F., 2001, *Nature*, **413**, 139
- Morscher M., Umbreit S., Farr W. M., Rasio F. A., 2013, *ApJ*, **763**, L15
- Morscher M., Pattabiraman B., Rodriguez C., Rasio F. A., Umbreit S., 2015, *ApJ*, **800**, 9
- O’Shaughnessy R., Gerosa D., Wysocki D., 2017, *Physical Review Letters*, **119**, 011101
- Pasquato M., Mapelli M., Giersz M., Askar A., 2018, Submitted to *MNRAS*
- Pavlík V., Jeřábková T., Kroupa P., Baumgardt H., 2018, *A&A*, **617**, A69
- Pedregosa F., et al., 2011, *Journal of Machine Learning Research*, **12**, 2825
- Peuten M., Zocchi A., Gieles M., Gualandris A., Hénault-Brunet V., 2016, *MNRAS*, **462**, 2333
- Portegies Zwart S. F., McMillan S. L. W., 2000, *ApJ*, **528**, L17
- Quinlan J. R., 1986, *Induction of decision trees*. Vol. 1, Springer
- Repetto S., Davies M. B., Sigurdsson S., 2012, *MNRAS*, **425**, 2799
- Repetto S., Igoshev A. P., Nelemans G., 2017, *MNRAS*, **467**, 298
- Richards J. W., et al., 2011, *ApJ*, **733**, 10
- Rish I., et al., 2001, in *IJCAI 2001 workshop on empirical methods in artificial intelligence*. pp 41–46
- Rodriguez C. L., Morscher M., Wang L., Chatterjee S., Rasio F. A., Spurzem R., 2016, *MNRAS*, **463**, 2109
- Roe B. P., Yang H.-J., Zhu J., Liu Y., Stancu I., McGregor G., 2005, *Nuclear Instruments and Methods in Physics Research Section A: Accelerators, Spectrometers, Detectors and Associated Equipment*, **543**, 577
- Servillat M., Webb N. A., Barret D., 2008, *A&A*, **480**, 397
- Shishkovsky L., et al., 2018, *ApJ*, **855**, 55
- Sigurdsson S., Hernquist L., 1993, *Nature*, **364**, 423
- Sippel A. C., Hurley J. R., 2013, *MNRAS*, **430**, L30
- Sokolova M., Japkowicz N., Szpakowicz S., 2006, in *Australasian joint conference on artificial intelligence*. pp 1015–1021
- Sollima A., et al., 2016, *MNRAS*, **462**, 1937
- Spera M., Mapelli M., 2017, *MNRAS*, **470**, 4739
- Spera M., Mapelli M., Bressan A., 2015, *MNRAS*, **451**, 4086
- Spitzer L., 1987, *Dynamical evolution of globular clusters*
- Steinwart I., Christmann A., 2008, *Support vector machines*. Springer Science & Business Media
- Stodolkiewicz J. S., 1982, *Acta Astron.*, **32**, 63
- Stodolkiewicz J. S., 1986, *Acta Astron.*, **36**, 19
- Strader J., Chomiuk L., Maccarone T. J., Miller-Jones J. C. A., Seth A. C., 2012, *Nature*, **490**, 71
- Taylor M. A., Puzia T. H., Gomez M., Woodley K. A., 2015, *ApJ*, **805**, 65
- Venables W. N., Ripley B. D., 2002, in *Modern Applied Statistics with S*. Springer, pp 251–269
- Vink J. S., de Koter A., Lamers H. J. G. L. M., 2001, *A&A*, **369**, 574
- Wang L., Spurzem R., Aarseth S., Nitadori K., Berczik P., Kouwenhoven M. B. N., Naab T., 2015, *MNRAS*, **450**, 4070
- Wang L., et al., 2016, *MNRAS*, **458**, 1450
- Weatherford N. C., Chatterjee S., Rodriguez C. L., Rasio F. A., 2018, *ApJ*, **864**, 13
- Webb J. J., Leigh N. W. C., Singh A., Ford K. E. S., McKernan B., Bellovary J., 2018, *MNRAS*, **474**, 3835
- Willems B., Henninger M., Levin T., Ivanova N., Kalogera V., McGehee K., Timmes F. X., Fryer C. L., 2005, *ApJ*, **625**, 324
- Wong T.-W., Valsecchi F., Fragos T., Kalogera V., 2012, *ApJ*, **747**, 111
- Wong T.-W., Valsecchi F., Ansari A., Fragos T., Glebbeek E., Kalogera V., McClintock J., 2014, *ApJ*, **790**, 119
- Wysocki D., Gerosa D., O’Shaughnessy R., Belczynski K., Gladysz W., Berti E., Kesden M., Holz D. E., 2018, *Phys. Rev. D*, **97**, 043014
- Zampieri L., Roberts T. P., 2009, *MNRAS*, **400**, 677
- Zhang Z., Gilfanov M., Bogdán Á., 2013, *A&A*, **556**, A9
- Ziosi B. M., Mapelli M., Branchesi M., Tormen G., 2014, *MNRAS*, **441**, 3703
- Zocchi A., Gieles M., Hénault-Brunet V., 2018, *MNRAS*, **478**, 100
- Zuo Z.-Y., 2015, *A&A*, **573**, A58

APPENDIX A: ADDITIONAL TABLES AND FIGURES

The Appendix contains the full set of data and predictions along with larger figures related to the machine learning classifier. In particular, the following tables and figures are presented:

Table A1 A full set of data and predictions from the *Harris (1996, updated 2010)* catalogue.

Table A2 A full set of data and predictions from the *Baumgardt & Hilker (2018)* catalogue.

Figure A1 Visualization of the decision tree classifier as presented in [subsection 3.4](#).

Figure A2 Visualization of decision boundaries within the decision tree classifier.

Table A1. Predictions for the presence of BH subsystems with data from the [Harris \(1996, updated 2010\)](#) catalogue.

Cluster Name	Half-Light Radius (pc)	Central Surface Brightness ($L_{\odot} \text{ pc}^{-2}$)	CVD ^a (km s ⁻¹)	Total V-band Luminosity (L_{\odot})	MRT ^b (Myr)	Observational Core Radius (pc)	BHS Prediction	BHS (Fallback)
NGC 104	4.15	6.44×10^4	11.00	5.01×10^5	3548.13	0.47	False	False
NGC 288	5.77	3.47×10^2	2.90	4.29×10^4	2089.30	3.50	True	True
NGC 362	2.05	4.37×10^4	6.40	2.01×10^5	851.14	0.45	False	False
NGC 1851	1.80	7.26×10^4	10.40	1.84×10^5	660.69	0.32	False	False
NGC 2808	2.23	3.38×10^4	13.40	4.88×10^5	1412.54	0.70	False	False
NGC 3201	4.42	9.14×10^2	5.00	8.17×10^4	1862.09	1.85	True	True
NGC 4590	4.52	1.09×10^3	2.50	7.59×10^4	1862.09	1.74	False	True
NGC 5139	7.56	6.87×10^3	16.80	1.09×10^6	12302.69	3.58	True	True
NGC 5272	6.85	8.03×10^3	5.50	3.05×10^5	6165.95	1.10	False	True
NGC 5286	2.48	1.18×10^4	8.10	2.68×10^5	1288.25	0.95	False	True
NGC 5466	10.70	8.26×10^1	1.70	5.30×10^4	5754.40	6.66	False	True
IC 4499	9.35	1.59×10^2	2.50	7.24×10^4	5370.32	4.59	True	True
NGC 5904	3.86	1.33×10^4	5.50	2.86×10^5	2570.40	0.96	False	True
NGC 5946	2.74	4.84×10^3	4.00	6.37×10^4	812.83	0.25	False	False
NGC 6093	1.77	3.29×10^4	12.40	1.67×10^5	630.96	0.44	False	False
NGC 6121	2.77	2.40×10^3	4.00	6.43×10^4	851.14	0.74	False	False
NGC 6171	3.22	9.66×10^2	4.10	6.03×10^4	1000.00	1.04	False	False
NGC 6205	3.49	8.41×10^3	7.10	2.25×10^5	1995.26	1.28	False	True
NGC 6218	2.47	2.09×10^3	4.50	7.18×10^4	741.31	1.10	True	True
NGC 6254	2.50	3.03×10^3	6.60	8.39×10^4	794.33	0.99	True	True
NGC 6256	2.58	2.54×10^3	6.60	6.19×10^4	724.44	0.06	False	False
NGC 6266	1.82	3.32×10^4	14.30	4.02×10^5	954.99	0.44	False	False
NGC 6284	2.94	1.05×10^4	6.30	1.31×10^5	1230.27	0.31	False	False
NGC 6293	2.46	1.87×10^4	7.70	1.11×10^5	870.96	0.14	False	False
NGC 6341	2.46	2.36×10^4	6.00	1.64×10^5	1047.13	0.63	False	False
NGC 6325	1.43	3.44×10^3	5.90	5.20×10^4	281.84	0.07	False	False
NGC 6342	1.80	5.93×10^3	5.20	3.16×10^4	323.59	0.12	False	False
NGC 6366	2.97	1.15×10^2	1.30	1.69×10^4	537.03	2.21	False	False
NGC 6362	4.53	6.87×10^2	2.80	5.15×10^4	1584.89	2.50	False	True
NGC 6388	1.50	5.82×10^4	18.90	4.97×10^5	794.33	0.35	False	False
NGC 6397	1.94	2.36×10^4	4.50	3.87×10^4	398.11	0.03	False	False
NGC 6441	1.92	4.18×10^4	18.00	6.08×10^5	1230.27	0.44	False	False
NGC 6522	2.24	1.82×10^4	6.70	9.82×10^4	724.44	0.11	False	False
NGC 6535	1.68	1.14×10^2	2.40	6.79×10^3	158.49	0.71	False	False
NGC 6541	2.31	2.43×10^4	8.20	2.19×10^5	1071.52	0.39	False	False
NGC 6558	4.63	9.31×10^3	3.10	3.22×10^4	1318.26	0.06	False	False
NGC 6624	1.88	2.71×10^4	5.40	8.47×10^4	512.86	0.14	False	False
NGC 6626	3.15	1.79×10^4	8.60	1.57×10^5	1479.11	0.38	False	False
NGC 6656	3.13	3.92×10^3	7.80	2.15×10^5	1698.24	1.24	True	True
NGC 6681	1.86	7.26×10^4	5.20	6.03×10^4	446.68	0.08	False	False
NGC 6712	2.67	1.16×10^3	4.30	8.55×10^4	891.25	1.53	False	True
NGC 6752	2.22	4.06×10^4	4.90	1.06×10^5	741.31	0.20	False	False
NGC 6779	3.01	2.13×10^3	4.00	7.87×10^4	1023.29	1.20	False	True
NGC 6809	4.45	6.56×10^2	4.00	9.12×10^4	1949.85	2.83	False	True
NGC 6838	1.94	4.58×10^2	2.30	1.50×10^4	269.15	0.73	False	False
NGC 6864	2.80	2.25×10^4	10.30	2.29×10^5	1412.54	0.55	False	False
NGC 6934	3.13	4.18×10^3	5.10	8.17×10^4	1096.48	1.00	True	True
NGC 7078	3.03	7.53×10^4	13.50	4.06×10^5	2089.30	0.42	False	False
NGC 7089	3.55	1.77×10^4	8.20	3.50×10^5	2511.89	1.07	False	True
NGC 7099	2.43	2.64×10^4	5.50	8.17×10^4	758.58	0.14	False	False
<i>(Less accurate models, those trained without Central Velocity Dispersion as a feature.)</i>								
1636-283	1.21	1.82×10^2	–	3.47×10^3	74.13	1.21	False	False
BH 176	4.95	1.65×10^1	–	3.60×10^3	616.60	4.95	False	False
E 3	4.95	2.09×10^1	–	3.80×10^3	630.96	4.41	False	False
HP 1	7.39	1.11×10^2	–	3.28×10^4	2754.23	0.07	False	False

Continued on next page

^aCentral Velocity Dispersion ^bMedian Relaxation Time

Table A1 – continued

Cluster Name	Half-Light Radius (pc)	Central Surface Brightness ($L_{\odot} \text{ pc}^{-2}$)	CVD ^a (km s^{-1})	Total V-band Luminosity (L_{\odot})	MRT ^b (Myr)	Observational Core Radius (pc)	BHS Prediction	BHS (Fallback)
IC 1276	3.74	8.33×10^1	–	3.98×10^4	1071.52	1.59	False	False
NGC 2298	3.08	1.00×10^3	–	2.86×10^4	691.83	0.97	False	False
NGC 4372	6.60	2.13×10^2	–	1.12×10^5	3890.45	2.95	True	True
NGC 4833	4.63	1.48×10^3	–	1.58×10^5	2630.27	1.92	False	True
NGC 5897	7.49	2.23×10^2	–	6.67×10^4	3715.35	5.09	True	True
NGC 5927	2.46	6.26×10^3	–	1.14×10^5	870.96	0.94	False	False
NGC 5986	2.96	3.11×10^3	–	2.03×10^5	1513.56	1.42	True	True
NGC 6101	4.70	2.79×10^2	–	5.11×10^4	1659.59	4.35	True	True
NGC 6139	2.50	4.80×10^3	–	1.89×10^5	1122.02	0.44	True	True
NGC 6144	4.22	3.47×10^2	–	4.70×10^4	1380.38	2.43	False	True
NGC 6235	3.35	8.18×10^2	–	2.81×10^4	776.25	1.10	False	False
NGC 6273	3.38	7.13×10^3	–	3.84×10^5	2398.83	1.10	False	True
NGC 6287	2.02	1.71×10^3	–	7.52×10^4	562.34	0.79	True	True
NGC 6304	2.44	4.80×10^3	–	7.11×10^4	707.95	0.36	False	True
NGC 6316	1.97	3.84×10^3	–	1.85×10^5	776.25	0.51	True	True
NGC 6333	2.21	4.03×10^3	–	1.29×10^5	794.33	1.03	True	True
NGC 6352	3.34	1.96×10^3	–	3.31×10^4	831.76	1.35	False	False
NGC 6355	2.36	3.20×10^3	–	1.45×10^5	912.01	0.13	False	False
NGC 6356	3.56	5.66×10^3	–	2.17×10^5	1995.26	1.05	False	True
NGC 6380	2.35	4.03×10^2	–	8.55×10^4	724.44	1.08	True	True
NGC 6401	5.89	1.20×10^3	–	1.24×10^5	3388.44	0.77	True	True
NGC 6402	3.52	1.57×10^3	–	3.73×10^5	2454.71	2.14	True	True
NGC 6426	5.51	3.35×10^2	–	3.98×10^4	1905.46	1.56	False	True
NGC 6440	1.19	5.46×10^3	–	2.70×10^5	416.87	0.35	True	True
NGC 6453	1.48	5.41×10^3	–	6.61×10^4	331.13	0.17	False	False
NGC 6496	3.35	3.11×10^2	–	6.49×10^4	1096.48	3.12	False	True
NGC 6517	1.54	3.44×10^3	–	1.71×10^5	524.81	0.19	False	True
NGC 6528	0.87	7.39×10^3	–	3.63×10^4	114.82	0.30	False	False
NGC 6539	3.86	1.35×10^3	–	1.77×10^5	2089.30	0.86	True	True
NGC 6544	1.06	1.09×10^4	–	5.11×10^4	173.78	0.04	False	False
NGC 6553	1.80	1.96×10^3	–	1.10×10^5	524.81	0.93	True	True
NGC 6569	2.54	2.00×10^3	–	1.75×10^5	1122.02	1.11	True	True
NGC 6584	2.87	3.23×10^3	–	1.02×10^5	1047.13	1.02	True	True
NGC 6637	2.15	6.81×10^3	–	9.73×10^4	660.69	0.84	False	False
NGC 6638	1.39	4.37×10^3	–	6.03×10^4	288.40	0.60	False	False
NGC 6642	1.72	6.81×10^3	–	3.94×10^4	331.13	0.24	False	False
NGC 6652	1.40	1.32×10^4	–	3.94×10^4	245.47	0.29	False	False
NGC 6717	1.40	7.13×10^3	–	1.57×10^4	165.96	0.17	False	False
NGC 6723	3.87	2.04×10^3	–	1.16×10^5	1737.80	2.10	True	True
NGC 6749	2.53	6.44×10^1	–	4.09×10^4	602.56	1.42	False	False
NGC 6760	2.73	1.25×10^3	–	1.17×10^5	1023.29	0.73	True	True
NGC 6981	4.60	8.97×10^2	–	5.60×10^4	1698.24	2.27	False	True
Pal 10	1.70	5.61×10^1	–	1.77×10^4	234.42	1.39	False	False
Pal 11	5.69	4.71×10^2	–	5.01×10^4	2187.76	4.64	True	True
Pal 12	9.51	7.53×10^2	–	5.25×10^3	1905.46	0.11	False	False
Pal 6	2.02	9.05×10^1	–	4.45×10^4	436.52	1.11	False	False
Pal 8	2.16	3.64×10^2	–	1.37×10^4	295.12	2.09	False	False
Terzan 1	7.44	3.35×10^0	–	4.97×10^3	1318.26	0.08	False	False
Terzan 10	2.62	1.12×10^2	–	2.96×10^4	549.54	1.52	False	False
Terzan 12	1.05	1.15×10^1	–	3.87×10^3	60.26	1.16	False	False
Terzan 2	3.32	4.98×10^1	–	1.92×10^4	660.69	0.07	False	False
Terzan 3	2.98	3.57×10^1	–	7.24×10^3	371.54	2.81	False	False
Terzan 5	1.45	1.35×10^2	–	7.94×10^4	338.84	0.32	False	True
Terzan 6	0.87	1.81×10^2	–	9.29×10^4	165.96	0.10	False	False
Terzan 7	5.11	1.98×10^2	–	8.63×10^3	912.01	3.25	False	False
Terzan 9	1.61	1.89×10^1	–	2.61×10^3	100.00	0.06	False	False
Ton 2	3.10	4.98×10^1	–	2.51×10^4	660.69	1.29	False	False

Table A2. Predictions for the presence of BH subsystems with data from [Baumgardt & Hilker \(2018\)](#) catalogue for Milky Way GC parameters.

Cluster Name	Half-Light Radius (pc)	Central Surface Brightness ($L_{\odot} \text{ pc}^{-2}$)	CVD ^a (km s^{-1})	Total V-band Luminosity (L_{\odot})	HMRT ^b (Myr)	Core Radius (pc)	BHS Prediction	BHS (Fallback)
NGC 104	3.56	5.58×10^4	12.20	4.40×10^5	3388.44	0.49	False	False
NGC 288	6.99	2.00×10^2	3.30	4.90×10^4	3801.89	4.78	False	False
NGC 362	2.32	2.36×10^4	8.80	2.09×10^5	1995.26	0.47	False	False
NGC 1851	1.65	1.57×10^5	10.20	1.50×10^5	1047.13	0.15	False	False
NGC 2298	2.96	1.61×10^3	1.60	2.52×10^4	301.99	0.78	False	False
NGC 2808	2.06	4.22×10^4	14.40	4.52×10^5	1621.81	0.68	False	True
E 3	5.45	3.11×10^1	1.80	3.79×10^3	1819.70	2.77	False	False
NGC 3201	3.77	9.93×10^2	4.70	6.21×10^4	2691.54	1.92	False	False
NGC 4372	6.34	5.67×10^2	4.90	1.32×10^5	5888.44	4.82	True	True
NGC 4590	4.51	7.85×10^2	3.70	6.09×10^4	3548.14	1.99	False	False
NGC 4833	6.61	2.76×10^3	4.80	2.96×10^5	4168.69	2.36	True	True
NGC 5139	7.04	5.72×10^3	17.60	1.22×10^6	24547.11	4.22	False	True
NGC 5272	3.36	1.04×10^4	8.10	2.53×10^5	2951.21	1.04	False	True
NGC 5286	2.64	1.82×10^4	9.30	2.84×10^5	1995.26	0.77	False	True
IC 4499	9.83	1.81×10^2	3.10	7.42×10^4	11481.55	5.30	True	True
NGC 5897	8.02	1.84×10^2	3.90	6.66×10^4	8317.64	5.85	True	True
NGC 5904	3.61	8.51×10^3	7.70	2.44×10^5	2570.39	1.19	True	True
NGC 5927	4.54	2.93×10^3	6.50	1.35×10^5	3019.95	1.45	True	True
NGC 5986	2.44	5.77×10^3	8.30	1.23×10^5	1318.26	1.09	False	True
NGC 6093	1.82	8.41×10^4	9.50	1.74×10^5	870.96	0.19	False	False
NGC 6121	2.82	4.44×10^3	4.70	5.64×10^4	954.99	0.67	False	False
NGC 6101	10.32	9.61×10^1	2.70	4.23×10^4	9549.92	5.45	False	True
NGC 6144	5.87	7.54×10^2	2.20	8.57×10^4	1737.80	2.72	True	True
NGC 6139	2.62	3.10×10^4	9.20	1.89×10^5	1905.46	0.41	False	False
Ter 3	5.27	7.14×10^1	2.40	7.09×10^3	2238.72	2.39	False	False
NGC 6171	3.11	2.22×10^3	4.20	4.02×10^4	891.25	0.87	False	False
ESO 452	3.50	1.36×10^3	1.60	3.15×10^3	501.19	0.14	False	False
NGC 6205	3.08	4.50×10^3	9.20	1.74×10^5	2290.87	1.58	True	True
NGC 6218	2.81	5.49×10^3	4.40	6.80×10^4	812.83	0.71	False	False
NGC 6254	2.78	5.55×10^3	6.20	9.48×10^4	1412.54	0.80	True	True
NGC 6256	2.97	3.63×10^4	4.40	3.23×10^4	933.25	0.06	False	False
NGC 6266	1.83	5.52×10^4	15.30	2.76×10^5	1348.96	0.38	True	True
NGC 6273	3.13	1.29×10^4	11.00	3.25×10^5	3388.44	1.11	False	True
NGC 6284	3.91	8.43×10^3	8.90	1.61×10^5	4677.35	0.63	False	False
NGC 6293	2.76	6.42×10^4	7.40	1.13×10^5	1479.11	0.12	False	False
NGC 6304	4.45	5.80×10^3	5.70	2.02×10^5	3090.29	1.02	False	True
NGC 6316	2.72	1.61×10^4	9.00	1.79×10^5	2089.29	0.59	False	False
NGC 6341	2.28	2.36×10^4	8.00	1.48×10^5	1737.80	0.61	False	False
NGC 6325	1.30	1.44×10^5	4.60	3.43×10^4	190.55	0.03	False	False
NGC 6333	2.10	6.06×10^3	9.90	1.23×10^5	1479.11	1.10	False	True
NGC 6342	2.12	3.99×10^4	4.50	1.64×10^4	354.81	0.06	False	False
NGC 6356	3.71	8.14×10^3	7.80	2.46×10^5	3467.37	1.14	False	True
NGC 6355	2.65	2.80×10^4	6.20	1.26×10^5	1230.27	0.33	False	False
NGC 6352	3.24	2.84×10^3	4.40	3.80×10^4	1174.90	0.62	False	False
NGC 6366	3.33	6.26×10^2	2.70	2.02×10^4	776.25	1.35	False	False
HP 1	2.56	6.13×10^3	5.50	2.20×10^4	912.01	0.29	False	False
NGC 6362	5.75	4.61×10^2	3.90	5.67×10^4	3311.31	2.87	False	False
Lil 1	1.05	1.05×10^7	25.70	4.52×10^5	371.53	0.02	True	False
NGC 6380	5.07	4.13×10^3	4.50	1.48×10^5	2951.21	0.99	False	True
Ter 12	1.95	2.24×10^3	2.80	1.93×10^3	186.21	0.09	False	False
Ton 2	4.46	4.62×10^2	2.90	1.51×10^4	1548.82	0.95	False	False
NGC 6388	1.96	1.33×10^5	18.20	5.49×10^5	1905.46	0.35	True	True
NGC 6402	3.57	5.46×10^3	11.10	3.52×10^5	3981.08	2.28	True	True
NGC 6397	2.19	3.64×10^4	5.20	4.08×10^4	912.01	0.08	False	False
Ter 5	1.12	3.26×10^5	18.90	4.31×10^5	363.08	0.19	True	False
NGC 6440	1.25	1.96×10^5	16.30	2.17×10^5	416.87	0.15	True	False
NGC 6441	2.03	1.09×10^5	18.80	6.00×10^5	2238.72	0.42	False	True
Ter 6	1.49	8.23×10^5	8.80	1.02×10^5	288.40	0.05	False	False
NGC 6453	9.61	2.41×10^2	2.80	6.57×10^4	7413.10	4.05	True	True
NGC 6496	5.05	2.98×10^2	3.40	3.80×10^4	2951.21	3.07	False	False

Table A2 – *continued*

Cluster Name	Half-Light Radius (pc)	Central Surface Brightness ($L_{\odot} \text{ pc}^{-2}$)	CVD ^a (km s ⁻¹)	Total V-band Luminosity (L_{\odot})	HMRT ^b (Myr)	Core Radius (pc)	BHS Prediction	BHS (Fallback)
NGC 6522	4.34	3.55×10^4	8.20	1.18×10^5	5623.41	0.15	False	False
NGC 6535	2.08	2.43×10^3	2.80	3.32×10^3	218.78	0.14	False	False
NGC 6528	1.97	3.52×10^4	6.30	3.97×10^4	467.74	0.12	False	False
NGC 6539	4.04	6.30×10^3	5.90	1.61×10^5	3162.28	0.91	False	False
NGC 6544	1.38	9.68×10^4	6.40	3.37×10^4	181.97	0.08	False	False
NGC 6541	2.61	1.06×10^5	8.70	1.94×10^5	1513.56	0.21	False	False
ESO 452	7.47	6.25×10^1	1.40	8.67×10^3	1862.09	2.64	False	False
NGC 6553	1.94	9.77×10^3	8.70	7.48×10^4	660.69	0.56	False	False
NGC 6558	1.77	1.20×10^4	3.50	2.78×10^4	181.97	0.24	False	False
IC 1276	3.28	1.29×10^3	3.50	2.74×10^4	954.99	0.92	False	False
Ter 1	2.28	6.95×10^3	7.80	6.93×10^4	977.24	0.60	False	False
NGC 6569	2.94	5.41×10^3	7.50	1.53×10^5	1949.84	1.21	True	True
NGC 6584	2.98	4.91×10^3	4.20	8.10×10^4	1318.26	0.72	False	True
NGC 6624	1.49	4.28×10^4	6.10	7.17×10^4	251.19	0.19	False	False
NGC 6626	1.76	3.71×10^5	12.70	1.68×10^5	776.25	0.13	False	False
NGC 6638	1.95	9.98×10^3	6.60	7.59×10^4	660.69	0.52	False	False
NGC 6637	2.70	1.19×10^4	8.00	2.38×10^5	1659.59	0.94	False	True
NGC 6642	1.50	5.12×10^4	7.00	4.92×10^4	234.42	0.13	False	False
NGC 6656	3.23	6.08×10^3	8.30	1.93×10^5	2691.54	1.26	True	True
NGC 6681	2.08	5.26×10^4	6.80	5.68×10^4	537.03	0.10	False	False
NGC 6712	2.87	3.26×10^3	5.00	9.00×10^4	1047.13	1.23	True	True
NGC 6715	3.20	8.52×10^4	16.20	6.91×10^5	5888.44	0.54	False	False
NGC 6723	3.50	2.09×10^3	5.20	8.85×10^4	1348.96	1.68	True	True
NGC 6749	3.38	1.20×10^3	3.20	3.92×10^4	954.99	1.28	False	False
NGC 6752	2.40	4.30×10^4	8.30	1.10×10^5	1445.44	0.19	False	False
NGC 6760	2.82	7.59×10^3	7.20	1.11×10^5	1737.80	0.75	False	False
NGC 6779	4.38	3.17×10^3	6.10	1.78×10^5	3090.29	1.71	True	True
NGC 6809	4.70	7.30×10^2	4.80	7.90×10^4	3235.94	2.93	False	True
Pal 11	6.63	2.61×10^2	3.70	6.55×10^4	4365.16	5.08	True	True
NGC 6864	2.46	2.25×10^4	11.80	1.99×10^5	2041.74	0.56	False	False
NGC 6934	2.63	2.48×10^3	4.70	6.65×10^4	1479.11	1.12	False	False
NGC 6981	4.31	8.44×10^2	3.20	5.88×10^4	1659.59	2.09	False	False
NGC 7078	1.90	2.45×10^0	12.90	3.94×10^5	1513.56	0.08	True	True
NGC 7089	3.00	2.24×10^4	10.60	3.59×10^5	2754.23	0.77	False	False
NGC 7099	2.44	6.65×10^4	5.50	7.19×10^4	1819.70	0.06	False	False
Pal 12	6.98	2.05×10^1	1.00	4.05×10^3	1513.56	3.70	False	False

^aCentral Velocity Dispersion ^bHalf-Mass Relaxation Time

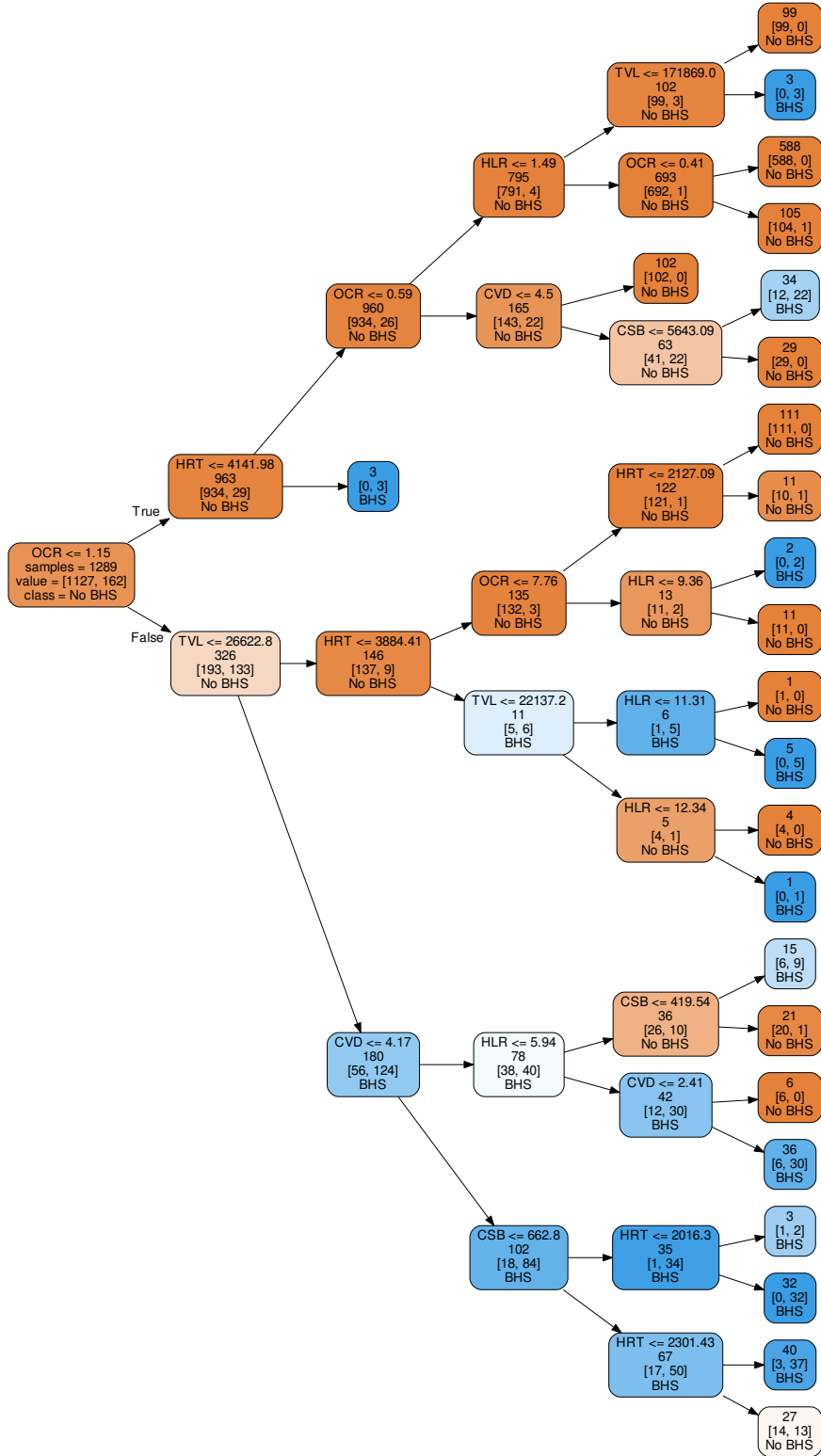


Figure A1. Visualization of decision tree. A legend is present at the root node. Nodes that are shaded blue are where the majority of examples contain a BHS. Nodes shaded orange are where the majority of example clusters do not contain a BHS.

HRT: Median Relaxation Time (Myr) CVD: Central Velocity Dispersion (km s^{-1})
 TVL: Total V-Band Luminosity (L_{\odot}) CSB: Central Surface Brightness (m pc^{-2})
 OCR: Observational Core Radius (pc) OHLR: Half-Light Radius (pc)

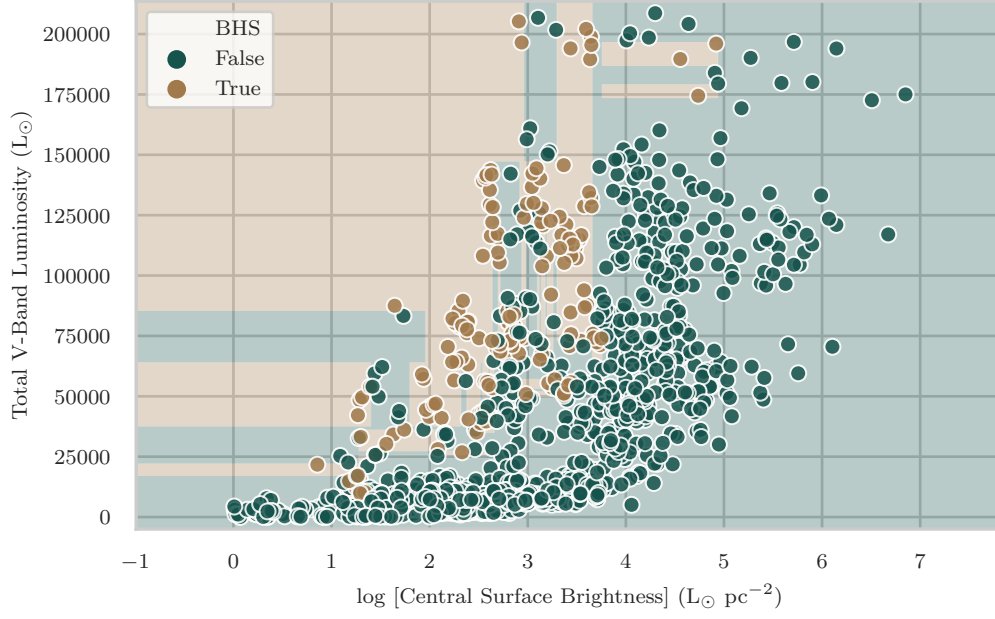


Figure A2. Decision boundaries (thresholds) for the two most important features in the decision tree classifier. The shading specifies where the classifier will predict that the cluster contains a BHS. Green shaded areas are where a prediction for no BHS will be given.

This paper has been typeset from a $\text{\TeX}/\text{\LaTeX}$ file prepared by the author.